Journal of Cleaner Production 365 (2022) 132707

Contents lists available at ScienceDirect

Journal of Cleaner Production

journal homepage: www.elsevier.com/locate/jclepro

Silk-based 2D nanocomposites for superior oily wastewater remediation

Mohamed K.M. Abd-Elbaki [a,1], Rehab M.G. Ahmed [b,1], Ahmed S.G. Khalil [b,c,*]

[a] Zoology Department, Faculty of Science, Fayoum University, 63514, Fayoum, Egypt
[b] Physics Department, Environmental and Smart Technology Group, Faculty of Science, Fayoum University, 63514, Fayoum, Egypt
[c] Materials Science and Engineering Department, School of Innovative Design Engineering, Egypt-Japan University of Science and Technology (E-JUST), 179, New Borg El-Arab City, Egypt

ARTICLE INFO

Handling Editor: M.T. Moreira

Keywords:
Natural silk fibers
Superhydrophobic
Plasma treatment
Oil/water mixture
Oil-in-water emulsions
Oily wastewater treatment

ABSTRACT

Oil spills hazard has increased along with the increase of industrial production, transportation and refining of oil. Therefore, it is becoming urgent to develop natural and efficient adsorbents for oily wastewater remediation. Herein, we report the development of superhydrophobic silk-based nanocomposites via plasma treatment followed by controlled surface decoration. The oxygen-plasma process was optimized to improve the surface properties and enhancing the adhesion of 2D nanomaterials on the natural silk fibers (SF). The SF was decorated with reduced graphene oxide (rGO) or molybdenum disulfide (MoS_2) nanosheets to obtain robust silk-based nanocomposites (rGO@PSF and MoS_2@PSF) with high oil selectivity. Detailed characterizations confirmed the presence of the composite structure with ultrathin coating of rGO or MoS_2 nanosheets over the entire surface of SF. The water uptake of the silk-based nanocomposites was substantially suppressed after the decoration with nanosheets. The silk-based nanocomposites showed outstanding chemical stability and durability after the exposure to several corrosive solutions and organic solvents. On the contrary, the pristine SF was chemically unstable hindering their applicability under harsh conditions. The rGO@PSF and MoS_2@PSF nanocomposites showed excellent oil adsorption capacity up to ~120 g/g and ~90 g/g for oil/water mixtures, respectively. In case of high concentration (up to 30 g/l) and highly stable oil-in-water emulsions, the composites demonstrated high adsorption capacity for crude, pump, and shell oil-in-water emulsions. rGO@PSF was more efficient than MoS_2@PSF in crude oil-in-water emulsion separation with an adsorption capacity up to 8203 and 8018 mg/g for rGO@PSF and MoS_2@PSF, respectively. Whereas MoS_2@PSF demonstrated a higher performance for pump oil-in-water emulsions separation with an adsorption capacity up to 3079 and 3529 mg/g for rGO@PSF and MoS_2@PSF, respectively. These differences in oil-in-water emulsions adsorption for both nanocomposites could be attributed to the materials flake size in relation to oil droplet size. Both silk-based nanocomposites exhibited excellent recyclability after ten adsorption cycles. Detailed separation mechanisms were introduced for the developed nanocomposites.

1. Introduction

Recently, the global demand for petroleum fuels has been increased owing to their important industrial and economical use (Gore et al., 2019a; Bhattacharyya and Andon, 2009). Throughout petroleum refining processes and sea transportation, liquid petroleum hydrocarbon leakage may accidently occur in the form of oil spills into the marine environment (Schrope, 2010). These oil spills are considered one of the most serious environmental concerns nowadays for their remarkable impact on the marine ecology and human society (Langangen et al., 2017; Conrad et al., 2021). Oil spills may occur in two forms, oil/water mixtures (two phases), and oil-in-water emulsions. Emulsions are known to have stable microdroplets (less than 20 μm) with complex wetting behavior (Gupta et al., 2016), hence, a large effort is required to separate emulsified oil-in-water compared to oil/water mixtures.

Natural oil spill cleanup is an unreliable and time-consuming process, and several methods have been developed such as skimming (Farooq and Ingrid, 2018), in-situ burning (Bullock et al., 2019), biodegradation (Prince and Butler, 2014; Ron and Rosenberg, 2014), air floatation (Saththasivam et al., 2016), gravitational separation (Gupta

* Corresponding author. Physics Department, Environmental and Smart Technology Group, Faculty of Science, Fayoum University, 63514, Fayoum, Egypt.
E-mail address: asg05@fayoum.edu.eg (A.S.G. Khalil).
[1] These authors equally contributed to this work.

https://doi.org/10.1016/j.jclepro.2022.132707
Received 24 January 2022; Received in revised form 5 May 2022; Accepted 12 June 2022
Available online 20 June 2022

et al., 2017) and membrane filtration (Yan et al., 2020; Abdel-Aty Ahmed et al., 2020). Although their extensive use over the past few years, these conventional methods still have limitations due to their poor separation efficiency, secondary pollution and/or high operational cost. Along with these methods, the use of sorbent materials such as carbon nanotube sponges (Zhu et al., 2013; Kukkar et al., 2020), polyurethane sponges (Xia et al., 2018; Zhou et al., 2016), melamine formaldehyde sponges (Peng et al., 2018; Zhou et al., 2019; Mao et al., 2021; Rehab et al., 2021), foams (Duan et al., 2021; Liu et al., 2021; Badawi et al., 2020; Mohammed et al., 2020) and aerogels (Wu et al., 2014; Long et al., 2021) has drawn a great attention in the recent years owing to its high adsorption capacity and ease of utility at the spill sites. Among these materials, the use of natural adsorbent materials such as wool (Radetic et al., 2008), corn straw (Tan et al., 2020), flax fiber (Liu et al., 2020a), nano-cellulose (Zhang et al., 2019), chestnut shell microfibers (Nine et al., 2020), Calotropis gigantea fibers (Xiao et al., 2021), and cotton fibers (Dashairya et al., 2018; Pal et al., 2019) is considered a promising approach for oil spill cleanup due to their low cost, non-secondary polluting, biocompatible, biodegradable nature.

For instance, Chen et al. prepared a hydrophobic/lipophilic cotton fabric modified by silica nanoparticles and showed an adsorption capacity of 71 g/g for crude oil (Chen et al., 2018). Liu et al. fabricated functionalized flax fiber that showed a good performance for oil/water separation (Liu et al., 2020b). In addition, Cao et al. developed metallic roughened Calotropis gigantea fibers by depositing Nickel and copper NPs onto the surface of fibers via a facile in-situ growth method (Cao et al., 2018). The metallic roughened fibers showed adsorption capacity of 45 and 120 g/g for ethanol and olive oil, respectively. Wang et al. prepared $NaClO_2$-modified cotton fabrics with separation efficiency up to 94.3% for toluene-in-water emulsions (Wang et al., 2017). These sorbent materials still have some limitations due to their quite low adsorption capacity and low selectivity towards heavy and high concentration oils. These drawbacks open the door for developing natural-based composite materials with high adsorption capacity, better selectivity and with non-secondary polluting nature.

Silk is an animal-derived fiber produced mainly from silkworms and is one of the most abundant biopolymers in nature (Chen and Porter Fritz, 2012a). It has been extensively used in textile industry and biomedical applications since the ancient history (Babu, 2018). Silk is composed of two main proteins, fibroin and sericin (Chen and Porter Fritz, 2012b). A single silk fiber is composed of two inner fibroin fibers coated by outer gummy sericin material that holds the two fibroin fibers together (Jao et al., 2016). Silk fibroin is a water non-soluble protein that resembles the core protein of the raw silk fiber (75–80%), hence, a degumming process should be performed to extract silk fibroin fibers and to remove the sticky sericin protein (Rockwood et al., 2011). Silk fibroin has been utilized in various biomedical applications owing to its biological properties as biocompatibility, biodegradability, and non-toxicity (Seo et al., 2007; Cao and Wang, 2009). In addition, it exhibits high mechanical strength, flexibility, and surface hydrophobicity (Gore et al., 2019b; Saric and Scheibel, 2019; Chen et al., 2019) making silk a potential candidate for oil/water separation. However, the water uptake of silk fibers may affect oil adsorbing selectivity during oil-water separation since the percentage of water uptake of silk fibers increases up to 53% after 60 min of immersion (YAMADA, 1998; Ta ş demir et al., 2010; Alam et al., 2011). Therefore, superhydrophobic modification is necessary for enhancing the hydrophobicity and reducing the water uptake of silk fibers, leading to better oil/water separation efficiency.

Over the last few years, many reports tried to tackle this issue. For instance, Patowary et al. chemically functionalized the SF by Octadecylamine (ODA) via a solution dip-coating technique (Patowary et al., 2016). The ODA functionalized SF exhibited superhydrophobicity of WCA ~150° ± 3°, and absorption capacity of 46.83 g g^{-1} and 84.14 g g^{-1} for crude oil and motor oil, respectively. Gore et al. explored the direct utilization of the degummed SF for efficient oil/water separation (Gore et al., 2019b). The Na_2CO_3 and water degummed SF exhibited oil/water separation efficiencies of 87.5% and 95%, respectively. Decoration the fibers with nanomaterials to enhance the hydrophobicity has been also explored in literature (Wang et al., 2018). Among the different types of these nanomaterials, reduced graphene oxide (rGO) and molybdenum disulfide (MoS_2), as two of the most common 2D materials, have been successfully used for surface hydrophobic modification of various materials for efficient oil water separation. RGO-coated cotton was investigated as a highly efficient adsorbent for oil/water separation, reached a WCA of ~162.9° and maximum oil sorption capacity (OSC) of ~30–40 g.g-1 (Dashairya et al., 2018). In another study, Zhou et al. prepared MoS_2-coated kapok fibers by a facile dipping method and the functionalized fibers showed excellent absorption capacity of (65 and 135) g/g for heptane and soybean oil, respectively (Zhou et al., 2020).

Plasma treatment is an eco-friendly technique used to modify the surface properties of many polymers and textile fabrics. Kodak et al. utilized sulfur hexafluoride (SF6) gas to impart a hydrophobic effect on the surface of SF. The deposition of the hydrophobic free fluorine species on the SF via fluorination increased the water contact angle up to 145° (Hodak et al., 2008). Wang et al. explored the effect of helium and oxygen plasma gas on the dyeability of SF. Plasma treatment by helium and oxygen as primary and secondary gases, respectively, increased the hydrophilicity and hence the dyeability of acid levelling dyes on SF (Wang et al., 2020; Jeong et al., 2009). This induced hydrophilicity may help increasing the adsorption of dyes, ions and enhancing the adhesion of nanomaterials onto the silk fibers. For instance, Rani et al. explored the surface modification of cotton fibers via oxygen plasma treatment to enhance the adhesion of graphene oxide onto the cotton fibers for electro-conductive properties. The cotton fibers pre-treated with glow discharge oxygen plasma showed an enhanced electrical conductivity compared to the untreated cotton fibers (Rani et al., 2018a).

Here, silk-based nanocomposites were developed via plasma treatment of natural SF followed by controlled decoration with GO and MoS_2 nanosheets using a facile immersion method. The oxygen plasma treatment introduced additional functional groups and enhanced the adhesion of the 2D nanosheets on the entire surface of SF. The developed silk-based nanocomposites showed high separation efficiency of several heavy (high concentration) oils and organic solvents as well as oil-in-water emulsions.

2. Experimental section

2.1. Materials

B.Mori silkworm cocoons were obtained from local supplier. Expandable graphite was obtained from Asbury Graphite Mills, USA. Sodium carbonate anhydrous (Na_2Co_3), potassium permanganate ($KMnO_4$), hydrogen peroxide (H_2O_2), sulfuric acid (H_2SO_4), ammonium molybdate tetrahydrate ($(NH_4)6Mo_7O_{24}{\cdot}4H2O$), thiourea, chloroform, toluene and n-hexane were purchased from Sigma Aldrich, Germany. Crude oil was obtained from Alpha resources LLC, USA. Shell (HX3) oil was obtained from local supplier. Pump oil was purchased from Petronuas Lubricants International. Deionized (DI) water was used in all experiments.

2.2. Synthesis of GO and MoS_2 nanosheets

The synthesis of graphene oxide from bulky graphite was performed via modified Hummer's method (Aboutalebi Hamed et al., 2011; Anis et al., 2017a). Briefly, dry expandable graphite was pre-treated at 1050 °C for 30 s to form expanded graphite (EG). Then, EG was added into concentrated H_2SO_4 with a ratio of (1:200 wt/V) and stirred continuously for 24 h 10 g of $KMnO_4$, oxidizing agent, were carefully mixed with the mixture under stirring. The mixture was let to cool in an ice bath. Then, DI water (200 ml) together with H_2O_2 (50 ml) were slowly added to the mixture (color changes to light brown). The mixture

was removed from the ice bath and transferred to room temperature for 30 min. After that, the mixture was washed with HCl solution (9:1 V_{water}/V_{HCl}) for three times. The produced GO was washed and centrifuged with DI water and ethanol, respectively, till the solution pH reaches about 6. GO powder was harvested by vacuum drying for 24 h at 70 °C.

MoS_2 was prepared according to the previously published protocol (Ali et al., 2019; Omar et al., 2019, 2021). Briefly, ammonium molybdate tetrahydrate (2.47 g) and thiourea (0.76 g) were dissolved into DI water (60 ml) with continuous stirring. Then, the mixture was moved into a Teflon-lined stainless-steel autoclave and placed in a drying oven at 200 °C for 24 h. After that the solution let to cool down to room temperature. The resultant precipitate was harvested by centrifugation, washed three times with DI water and ethanol, and dried in an oven at 80 °C for 12 h. Thermal treatment was performed in a tube furnace at 800 °C for 2 h under Ar gas atmosphere to form 2H–MoS2.

2.3. Degumming of silk fibers

The silk cocoons were chopped into small pieces (4–5 pieces), then 5 g of cocoons were boiled in sodium carbonate aqueous solution (0.05 wt %) for 60 min at 100 °C. The degummed silk fibers were squeezed to remove the excess of water and rinsed for 20 min with DI water for three times and air-dried at room temperature overnight.

2.4. Oxygen plasma treatment and weight loss (%) calculation

The as-degummed silk fibers were treated utilizing plasma system (AutoGlow200, Glow Research, USA) as follows: the SF were placed into the reactor chamber, which was then vacuumed at 0.1 torr, SF were treated using oxygen gas plasma with an exposure time of 10 min, an operating pressure of 1.0 torr and different treatment power of (50, 100, 150, 200 and 250) watt. Weight loss percentage of the plasma treated SF (PSF) was calculated using the following equation:

$$\textit{Wight loss}\ (\%) = \frac{W1 - W2}{W1} \times 100 \quad (1)$$

where w_1 and w_2 are the weight of the SF before and after plasma treatment, respectively. Each experiment was repeated three times and the mean values and standard errors were estimated.

2.5. Preparation of superhydrophobic silk-based nanocomposites

Superhydrophobic silk-based nanocomposites were prepared via plasma treatment followed by a facile immersion method (Scheme 1). Briefly, GO and MoS_2 solutions (2 mg/ml) were prepared by ultrasonication of the desired amounts of GO and MoS_2 in DI water. The plasma treated silk fibers (PSF) were immersed into GO or MoS_2 dispersions for 12 h and dried at 70 °C to obtain highly stable decorated SF (GO@PSF or MoS_2@PSF). Thermal reduction process was performed for GO@PSF at 120 °C for 5 h to obtain reduced graphene oxide decorated silk fibers (rGO@PSF).

2.6. Water uptake of SF and silk-based nanocomposites

Water uptake experiments of degummed SF as well as silk-based nanocomposites were performed by immersing the fibers into a beaker contains 50 ml of DI water for up to 120 min at room temperature (Alam et al., 2011; Xu et al., 2010a). The water excess on surface of the fibers was carefully eliminated before weighing. The water uptake percentage was estimated following the same steps reported in literature (Alam et al., 2011; Xu et al., 2010b).

2.7. Characterization of materials

The structure and morphology of GO, MoS_2 nanosheets, SF, rGO@PSF and MoS_2@PSF were investigated via HR-SEM (SEM, ZEISS Sigma 500 VP, coupled with EDX detector) and transmission electron microscopy (TEM, JEOL 1200).

X-ray diffraction (XRD) patterns were obtained by D8 ADVANCE diffractometer using Cu Ka monochromatic radiations at room temperature to investigate the structure of the prepared GO and MoS_2 nanosheets.

XPS analysis of SF, PSF, rGO@PSF and MoS_2@PSF was collected on

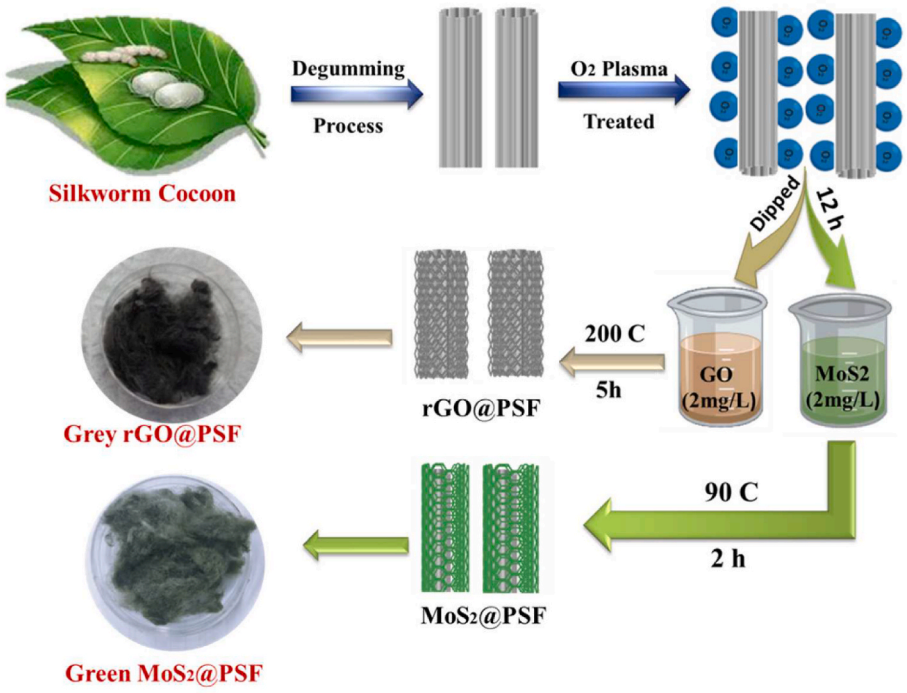

Scheme. 1. Illustration of the process steps used for the development of the superhydrophobic silk-based nanocomposites.

K-ALPHA (Themo Fisher Scientific, USA) with monochromatic X-ray Al K-alpha radiation, spot size 400 μm at pressure 10^{-9} mbar with full spectrum pass energy 200 eV and at narrow spectrum 50 eV. Raman spectrums were investigated via (WITec alpha 300 RA confocal Raman microscopes) with 50 x objective. Each sample was excited by a 532 nm Nd: YAG laser at room temperature.

UV–Vis spectra were measured by Carry 60 spectrophotometer. Surface functionalities were analyzed using Fourier transform infrared spectroscopy (FTIR, Jasco6000).

Contact angle (CA) measurements were analyzed using Dataphysics system (OCA 25 Plus, Germany) with sessile drop method. Droplet size distribution and zeta potential of oil-in-water emulsions were measured by Zetsizer Nano (Malvern, UK).

Optical microscopy images were captured via (Zeiss, Axio Vert.A1) microscope to qualitatively analyze the feed and permeate of oil-in-water emulsions. Moreover, chemical oxygen demand (COD) measurement was utilized to quantitatively evaluate permeate purity after the separation process.

2.8. Oil sorption experiments

2.8.1. Adsorption of immiscible oil/water mixtures

The ability of the rGO@PSF and MoS_2@PSF to remove oil from water was investigated as follows; oil/water mixtures of several oils and organic solvents such as shell oil, pump oil, toluene, chloroform, and n-hexane, were prepared with a volume ratio of 1:4 (Voil/Vwater). The pristine and silk-based nanocomposites (SF, rGO@PSF and MoS_2@PSF) were immersed into the mixture for 3 min, then, the fibers were taken out from the mixture. Oil sorption capacity (OSC) is the weight of adsorbate (oil or organic solvent) taken up by the adsorbent (SF or nanocomposites) per unit mass (g/g) and calculated according to the following formula:

$$\textit{Oil Sorption capacity}\ (\frac{g}{g}) = \frac{W2 - W1}{W1} \quad (2)$$

where W1 and W2 are the weight of fibers before and after adsorption (g), respectively. All calculations of OSC were repeated for three times to estimate the error bar.

2.8.2. Formulation of oil-in-water emulsions

Surfactant-free emulsions were prepared using a high-energy ultrasonication process. Briefly, three types of surfactant-free emulsions were formulated by mixing the desired amounts of DI water and oils (crude oil, pump oil and shell oil) to prepare different concentration of oils (10 g/l and 30 g/l) at pH (5.5–6), then the mixture was treated using ultrasonic horn (model VCX750) with an operating power of 525 W for 30 min. To avoid the effect of temperature, an ice bath was used for cooling the sample during sonication. The characteristics of the as-prepared oil-in-water emulsions are listed in Table 1. The stability of the prepared crude and pump, and shell oil-in-water emulsion was evaluated by DLS over 7 days without notable increase in the droplet size (Fig. S1).

Table 1
Characteristics of the oil-in-water emulsions.

Test oil	Concentration of oil (g/l)	COD of feed emulsions (mg/l)	Droplet size of fresh emulsions (nm)	Droplet size (nm) after one day
Crude oil	10	13500	717 ± 105	792 ± 25
	30	33300	1162.33 ± 102	1278 ± 30
Pump oil	10	10430	105 ± 14	107 ± 13
	30	23000	132 ± 11	145 ± 10
Shell oil	10	4980	144 ± 17	150 ± 20
	30	17250	210 ± 30	220 ± 25

2.8.3. Adsorption experiments of oil-in-water emulsions

The separation of the nanosized oil droplets from the emulsion was carried as follows; a certain amount (~0.22) g of the fibers was immersed in 50 ml of an emulsion. The emulsion was kept at a temperature of 318 K and stirred at 500 rpm for 4 h. For the kinetic experiments, the concentration of emulsion at different adsorption time was measured by COD. OSC of the fibers was evaluated using the following equation:

$$Qt\ (mg.g^{-1}) = (C_0 - C_t)\ V/m \quad (3)$$

Where C_0 and C_t are COD values of the initial and different time-emulsion concentrations respectively, m is the mass of the fibers (g), and V is the used emulsion volume (l). Emulsion separation efficiency was calculated as follows:

$$\text{Separation efficiency}\ (\%) = C_0 - C_e/C_0 \times 100 \quad (4)$$

3. Results and discussion

3.1. Characterization of GO and MoS_2 nanosheets as well as silk-based nanocomposites

High resolution scanning and transmission electron microscopy were used to investigate the morphology of GO and MoS_2 nanosheets (Fig. S2). GO nanosheets consisted of exfoliated and wrinkled thin sheets (Figs. S2A and D) confirming the successful exfoliation of bulk graphite oxide (Geng et al., 2009). Fig. S2B showed the flower-like MoS_2 nanosheets and their characteristic monolayer structure (Fig. S2E).

UV–Vis spectrum of GO dispersion was illustrated in Fig. S3A. The spectrum exhibited two bands at 230 and 300 nm corresponding to the π–π* transitions of the aromatic c–c bond and the n–π* transitions of C=O bonds, respectively (Sun et al., 2008). The UV–Vis spectrum of MoS_2 nanosheets (Fig. S3B) showed absorption peaks at 628 and 667 nm that can be attributed to the Brillouin zone excitation at the K point of the 2H phase (Qi et al., 2016; Benavente et al., 2002). Figs. S3C–D showed the size distribution of GO and MoS_2 nanosheets respectively. The characteristic peaks were found at 180 nm and 70 nm for GO and MoS_2 nanosheets respectively, indicating the efficient exfoliation of both dispersions. 2H–MoS_2 nanosheets can be easily exfoliated and resulted in a green suspension (Chang et al., 2016; Geng et al., 2016). The appearance of the green color of MoS_2@PSF and the gray color of rGO@PSF nanocomposites (Scheme 1), confirm the successful decoration of both nanosheets on the entire surface of SF.

Fig. 1 shows the morphology and microstructure of the pristine SF and the silk-based nanocomposites. The SEM images of the pristine SF with a smooth surface were shown in Fig. 1A, D. In addition, SEM images of PSF indicated no change in the fibers' morphology (Fig. S2 C, F). However, after decoration with rGO and MoS_2 nanosheets (Fig. 1B, E and Fig. 1C, F), uniform hierarchical structures on the SF were observed, which more likely endows the surface roughness. These silk-based nanocomposites attained superhydrophobicity allowing high oil/water separation performance as described below.

EDX mapping (Fig. 1G–I) indicated that the rGO@PSF mainly composed of oxygen and carbon, uniformly distributed over the SF surface. In addition, Fig. 1G–I shows the EDX mapping of the MoS_2@PSF, containing molybdenum and sulfur, which are uniformly distributed over the SF surface. These results illustrate the successful deposition of rGO and MoS_2 nanosheets on the entire SF surface.

Attenuated total reflection infrared (ATR-IR) spectroscopy was utilized to characterize the GO and rGO powder samples (Fig. S4A). The resulted peaks at 1059 cm^{-1} could be attributed to epoxy C–O and alkoxy C–O stretching bands. In addition, the peaks at 1429, 1725 and 3230 cm^{-1} in the GO spectrum may be attributed to C–OH, C=O, and O–H stretching bands, respectively. Absorption peak at 1625 cm^{-1} could

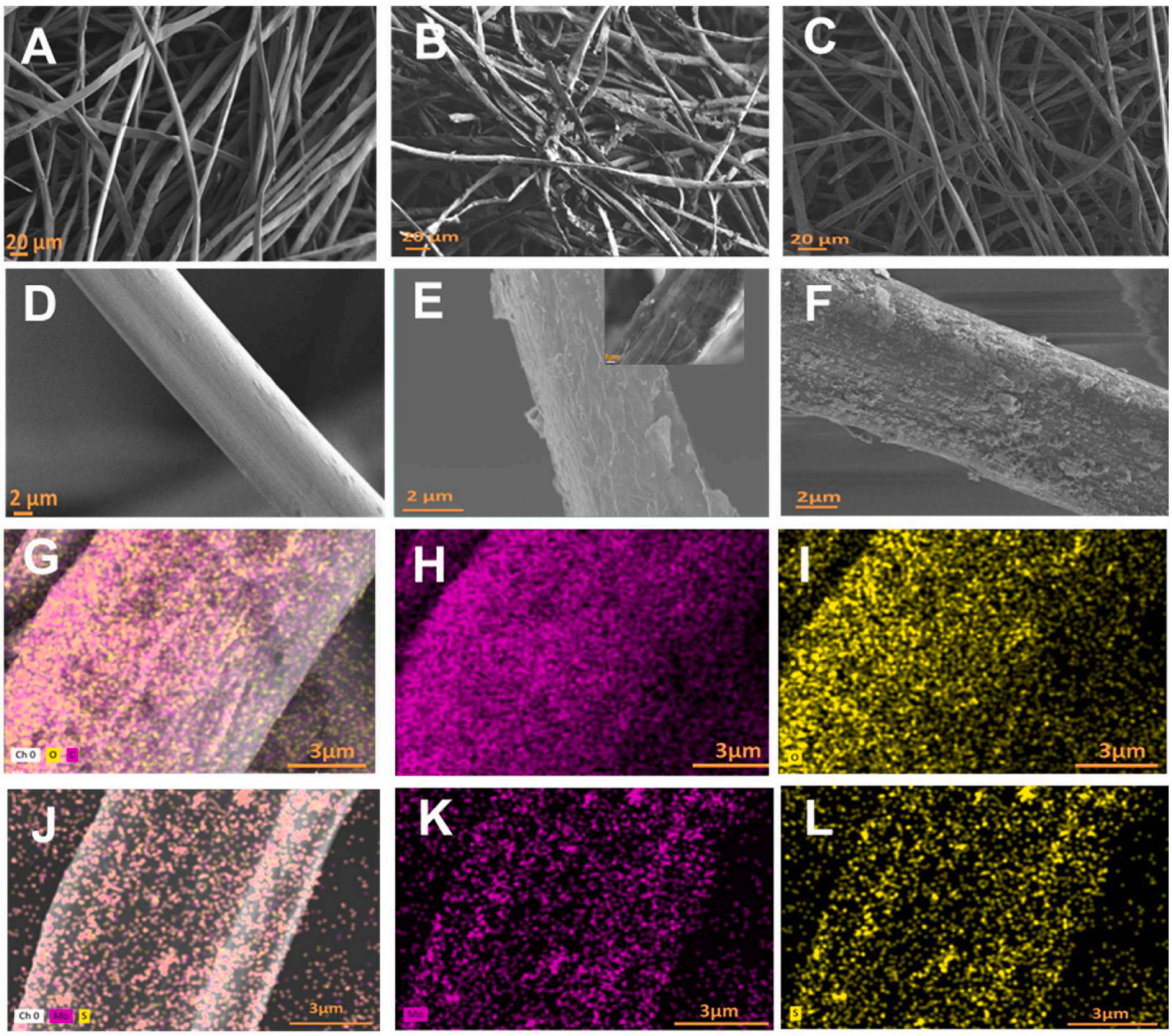

Fig. 1. SEM and EDX elemental mapping images of the pristine and silk-based nanocomposites. (A, D) SF, (B, E) rGO@PSF, and (C, F) MoS_2@PSF at low and high magnifications, respectively. (G–I) EDX elemental mapping images of rGO@PSF and (J–L) EDX elemental mapping images of MoS_2@PSF.

be corresponding to the aromatic ring C–C vibration. However, after thermal reduction, the rGO sample showed the disappearance of all oxygen functional groups excluding the vibration of aromatic ring C=C bond at 1625 cm^{-1} (Thema et al., 2013).

The Raman spectra of 2H–MoS_2, GO, rGO, SF, and silk-based nanocomposites were recorded in Fig. 2. Raman spectrum of SF showed adsorption peaks at 1082 cm^{-1}, 1228 $cm^{-1}$and 1662 cm^{-1} which are characteristic for β-sheet secondary structure (Monti et al., 1998). The 2H–MoS_2 powder and MoS_2@PSF showed adsorption peaks at 380 and 405 cm^{-1} attributed to E12g and A1g vibration modes of the 2H–MoS2 (He et al., 2019; Yu et al., 2018) indicating that 2H–MoS_2 was successfully decorated on the SF surface. Raman spectra of GO, rGO, and rGO@PSF exhibited two characteristic spectral peaks around 1346 and 1581 cm^{-1}, corresponding to the disorder defective band (D) and graphitic band (G), respectively (Anis et al., 2017b). The intensity ratios of D to G band (ID/IG) of GO and rGO were 0.95 and 0.98, respectively.

XPS analysis of the pristine and silk-based nanocomposites was shown in Fig. 3. All samples displayed the main elements of carbon (C1s), oxygen (O1s) and nitrogen (N1s). The relative intensity of O1s peak of PSF shows higher value than SF indicating the oxidation resulted from oxygen plasma (Fig. 3A and B). In case of rGO@PSF (Fig. 3D), the relative intensity of O1s obviously decreased and C1s increased after thermal reduction of GO into rGO. In addition, the relative intensity of N1s decreased representing the complete decoration of SF by rGO nanosheets. The XPS spectrum of MoS_2@PSF shows the characteristic peaks of molybdenum disulfide (Mo3d and S2p) declaring the successful decoration of MoS_2 nanosheets on SF (Fig. 3E).

To further explore the effect of plasma treatment on the surface chemistry of SF, XPS C1s high resolution profiles of SF and PSF were shown in Fig. 3C,F. Different functional groups of the main carbon skeleton (C–C) bond at 284.78 eV, the carbonyl carbon (C=O) at 287.6 eV and the carbon in (C–N/C–O) at 286.1 eV were shown in both samples with the introduction of a new peak (O–C=O) at 288.9 eV for the plasma treated SF (Fig. 3F). Similar results were reported by oxygen plasma treatment of cotton fibers (Rani et al., 2018b).

3.2. *Effect of plasma treatment*

Oxygen plasma treatment was applied on the surface of the pristine SF to enhance the adherence of both the MoS_2 and GO nanosheets. This strong and stable adherence may be attributed to the interaction between –OH, -NH2, –C=O, and –COOH functional groups induced by the oxygen plasma on the surface of SF and the hydrophilic functional groups present in case of GO nanosheets or the sulfur functional groups in case of MoS_2 nanosheets (Fang et al., 2008; Ma et al., 2018; Zulan et al., 2019). The optimization of plasma treatment power was carried out on the SF. Fig. 4A shows the effect of plasma power on the weight of the PSF (represented by weight loss %). Exposing the SF to plasma power of 50W and 100W resulted in a weight loss of 7% and 14.2%, respectively, while treatment at higher power of 150W, 200W and 250W

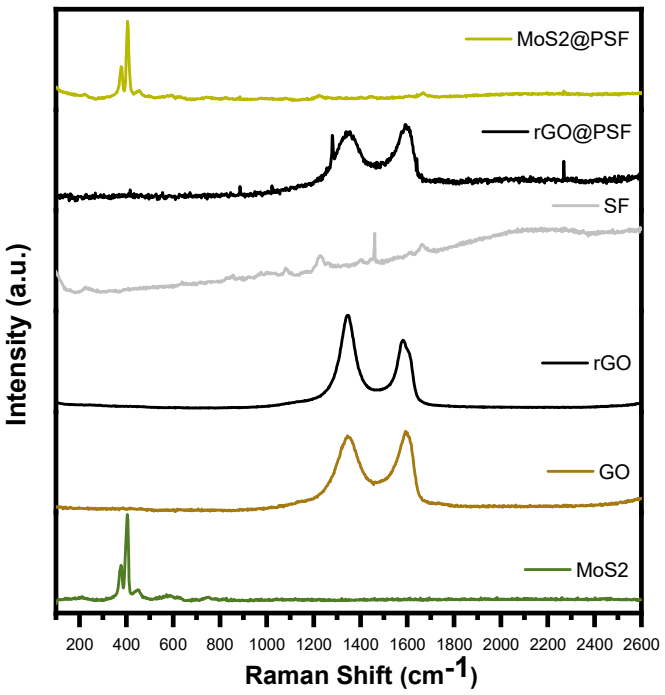

Fig. 2. Raman spectra of MoS_2, GO and rGO nanosheets as well as SF, rGO@PSF and MoS_2@PSF nanocomposites.

resulted in weight loss of 17.1%, 18.3% and 22.57%, respectively.

Fig. 4B shows the effect of plasma power on the OSC of the plasma-treated SF decorated with rGO and MoS_2. Pump oil (here, it was just taken as an example oil to explore the optimum conditions for further separation experiments) sorption capacities were 108 g g^{-1} and 78 g g^{-1} for rGO@PSF and MoS2@PSF, respectively at the plasma power of 50W. Where it increased to 130 g g^{-1} and 79 g g^{-1} at 100W. Moreover, the OSC decreased with further increase of the plasma treatment power (at 150W, 200W and 250W). Based on the results shown in Fig. 4, one can conclude that the SF treated at plasma power of 100 W owns the highest OSC and most reasonable weight loss.

3.3. Surface wettability analysis

An excellent oil adsorbent should possess superhydrophobic property. Therefore, contact angle measurements were performed on the pristine and the silk-based nanocomposites to explore their capability for oil-water separation applications. Fig. 5 shows the wettability behavior of the pristine and silk-based nanocomposites. Water contact angle (WCA) measurements (Fig. 5A) showed that SF has a WCA of ~120° indicating the intrinsic hydrophobic nature of SF. The WCA of MoS_2@SF and rGO@SF (without plasma treatment) were 136° and 147°, respectively. After plasma treatment, the MoS_2@PSF and rGO@PSF showed WCA of 150° and 160°, respectively, illustrating the excellent effect of plasma treatment on the adherence of GO and MoS_2 nanosheets on the SF.

Moreover, these wetting behaviors were confirmed by taking digital photographs of water droplets on the surface of SF, PSF, rGO@PSF and MoS_2@PSF. The pristine SF (Fig. S5A) showed relatively low hydrophobicity. However, PSF showed superhydrophilicity induced by oxygen plasma treatment (Fig. S5B). Both MoS_2@PSF and rGO@PSF (Figs. S5C–D) showed excellent superhydrophobicity. For better visualization, the water droplets were dyed with methylene blue dye.

To further investigate the durability of rGO@PSF and MoS_2@PSF nanocomposites, the chemical stability was examined after the exposure to several corrosive solutions and organic solvents (Fig. 5B–D). The WCA was monitored for all samples. Fig. 5B showed the stability of SF, rGO@PSF and MoS_2@PSF after exposure to n-Hexane, toluene, and chloroform for 12 h. Fig. 5C–D showed the stability of rGO@PSF and

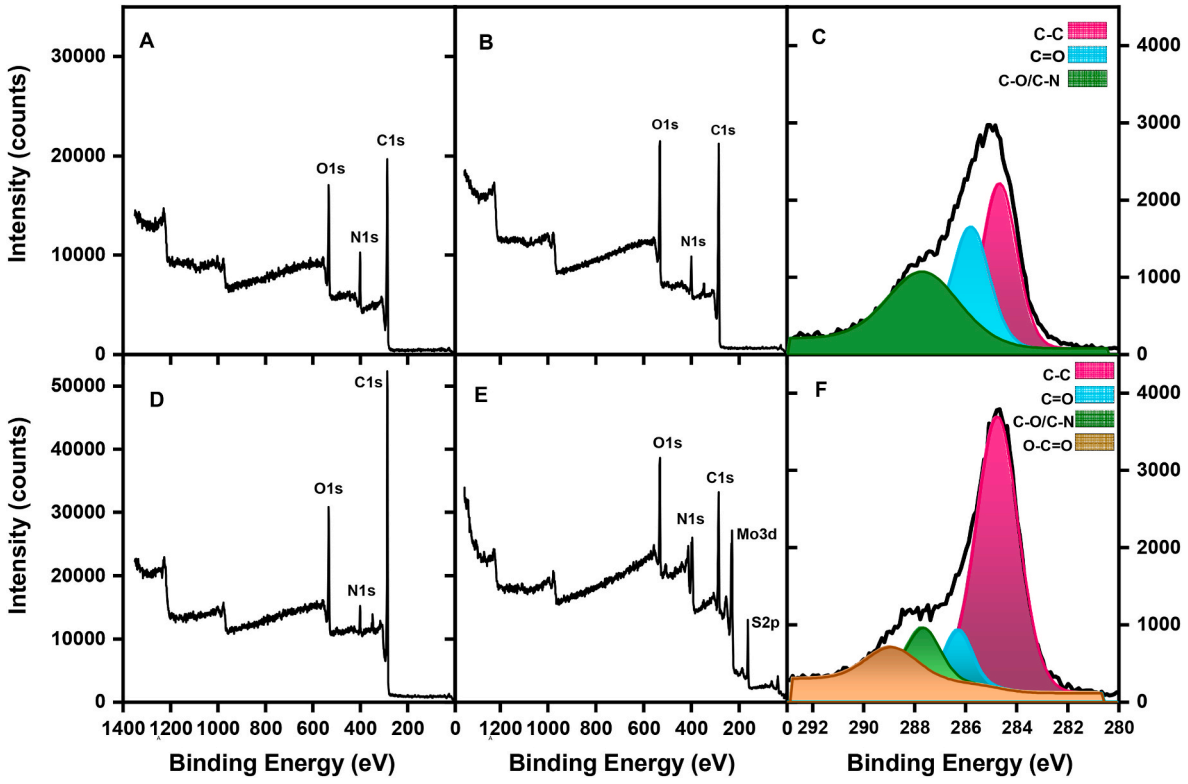

Fig. 3. XPS analysis of the pristine, plasma-treated, and silk-based nanocomposites. (A, B, D, E) Survey spectra of SF, PSF, rGO@PSF and MoS_2@PSF, respectively. (C, F) High resolution C1s profiles of SF and PSF, respectively.

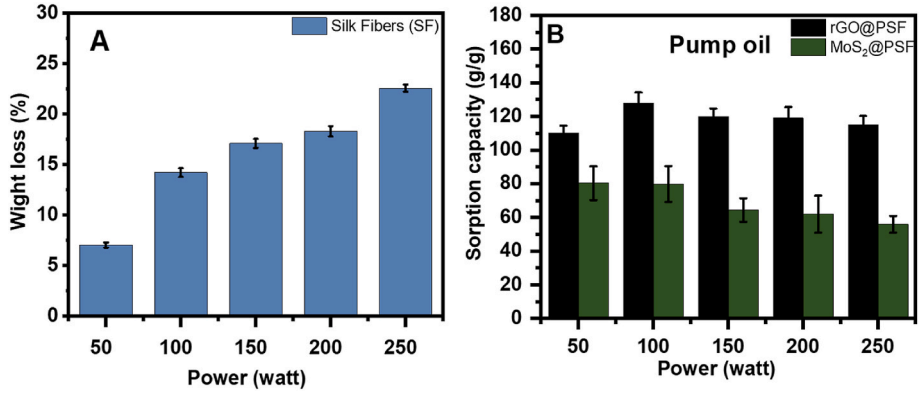

Fig. 4. The effect of plasma power on A) The weight of SF and B) Oil sorption capacity of silk-based nanocomposites.

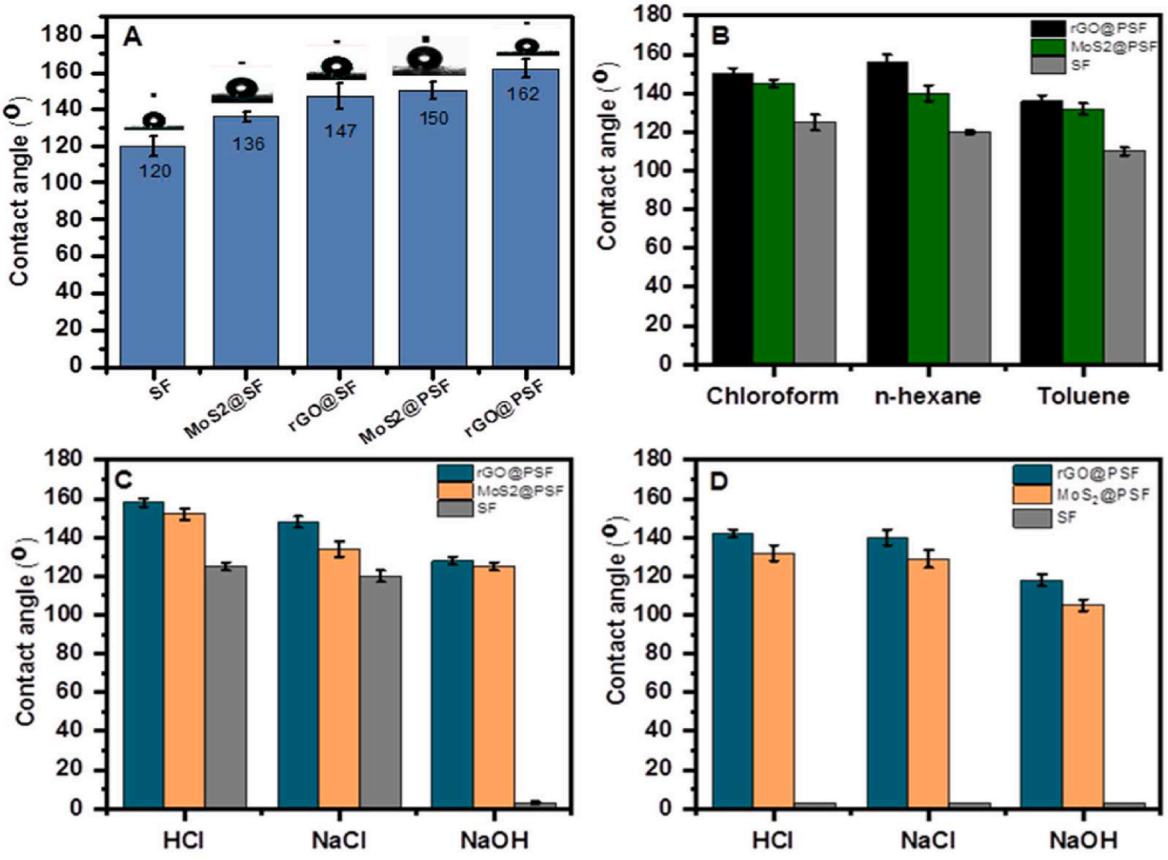

Fig. 5. Surface wettability analysis of the pristine and silk-based nanocomposites. (A) Water contact angle measurements. Water contact angle measurements of the pristine and silk-based nanocomposites after exposure to (B) organic solvents, (C–D) various corrosive solutions with concentration of 0.01M and 1M, respectively for 12 h.

MoS_2@PSF after immersing into 0.1M and 1M, respectively of HCl, NaCl, and NaOH aqueous solutions for 12 h. In case of SF, the immersion in solutions (HCl and NaCl) at low concentration of 0.1M, caused a slight decrease in WCA, however, the NaOH treatment partially degraded the SF. Moreover, the immersion of SF in corrosive solutions at high concentration of 1M completely degraded the SF (WCA cannot be measured, here denotes as zero). These results confirm the instability of SF in alkali and corrosive solutions and can be attributed to the extensive depolymerization of SF molecules leading to degraded lower molecular weight peptides or amino acids (Wang et al., 2021; Ren et al., 1997). On the other hand, rGO@PSF and MoS_2@PSF nanocomposites demonstrated a slight decrease in WCA values. These results firm up the superhydrophobicity and chemical stability of rGO@PSF and MoS_2@PSF nanocomposites even under extreme conditions. This may be attributed to the hydrophobic stability and the strong adhesion of rGO and MoS_2 nanosheets on the SF, achieved after the plasma treatment.

Water uptake experiments of degummed silk fiber was performed by immersing the fibers into a beaker contains 50 ml of DI water for 120 min at room temperature. It was observed that pure silk fibroin can absorb up to 37.16 ± 1.5 g.g-1. However, this value was reduced by 26.75% and 72.71% in case of MoS_2@PSF and rGO@PSF, respectively. These results can be attributed to the successful decoration of the nanosheets on the entire surface of the fibers, leading to the

enhancement of the hydrophobicity.

3.4. Separation of oil/water mixtures

OSC of the pristine and the silk-based nanocomposites (SF, rGO@PSF and MoS_2@PSF) were studied to investigate their applicability to remove different oils and organics solvents (Fig. 6). As illustrated in Fig. 6A, the silk-based nanocomposites displayed high selectivity towards oil. By immersing rGO@PSF into an oil/water mixture, the fibers were able to successfully remove the oil from water within few seconds. Moreover, the separation of oil/water mixtures was expressed by OSC measurements shown in Fig. 6B. OSC of the tested samples without plasma treatment (SF, rGO@SF and MoS_2@SF) for different oils and organic solvents were shown in Fig. S6. The OSC in case of pump oil was 66.7, 65.1 and 99.2 g g^{-1} for SF, MoS_2@SF and rGO@SF, respectively (Fig. S6). Whereas, it was observably increased to 72.2 and 124.6 g g^{-1} for MoS_2@PSF and rGO@PSF, respectively (Fig. 6B). The apparent differences of OSC for oils and organic solvents could be attributed to the difference in their density and viscosity. The OSC of MoS_2@PSF and rGO@PSF exhibited higher values than those reported for other similar adsorbent materials (Table 2). These results were attributed to the superhydrophobic property possessed by the hierarchical nanosheet structure on the surface of SF allowing large surface area during the adsorption process.

The recyclability of the pristine and silk-based nanocomposites was studied to investigate their practical oil spill cleanup application. Shell oil and toluene water mixtures were utilized to analyze the recyclability with a quick adsorption and a simple mechanical squeezing followed by hexane washing and drying at 100 °C for up to ten cycles. Fig. 6C–D shows the OSC variation for toluene and shell oil over ten cycles. In case of toluene, the OSC of the fibers shows a slight decrease after each consecutive cycle. The OSC was 30, 27 and 39 g g^{-1} for SF, MoS_2@PSF and rGO@PSF, respectively after ten cycles. However, in the case of shell oil, the OSC shows a significant decrease after each consecutive cycle. The OSC was 31, 48 and 53 g.g-^{1} for SF, MoS_2@PSF and rGO@PSF, respectively after ten cycles. The difference in the recyclability values between toluene and shell oil could be mainly attributed to the ease of toluene cleaning after adsorption due to its volatile nature. In contrast, oil droplets retain in the form of oil residues on the surface of SF even after extensive washing by n-hexane.

3.5. Separation of oil-in-water emulsions

Separation of oil in-water emulsions using the pristine and the silk-based nanocomposites was studied in detail. Several factors of emulsion properties such as type of oil, concentration of oil and average droplet size were studied in relation to OSC. The average oil droplet size and COD values of oil-in-water emulsion were evaluated at different oil content (10 and 30 g/l).

3.5.1. Effect of contact time, emulsion concentration and temperature

Emulsions are tiny oil droplets dispersed in water and hard to be removed due its high stability than the immiscible oil/water mixtures. To investigate the capability of the pristine and the silk-based nanocomposites to efficiently separate oil-in-water emulsions, crude, pump, and shell oil-in-water emulsions were formulated with different concentrations (10 and 30 g/l) and tested while maintaining a constant temperature of 318 K for different contact time (0–4h). Adsorption

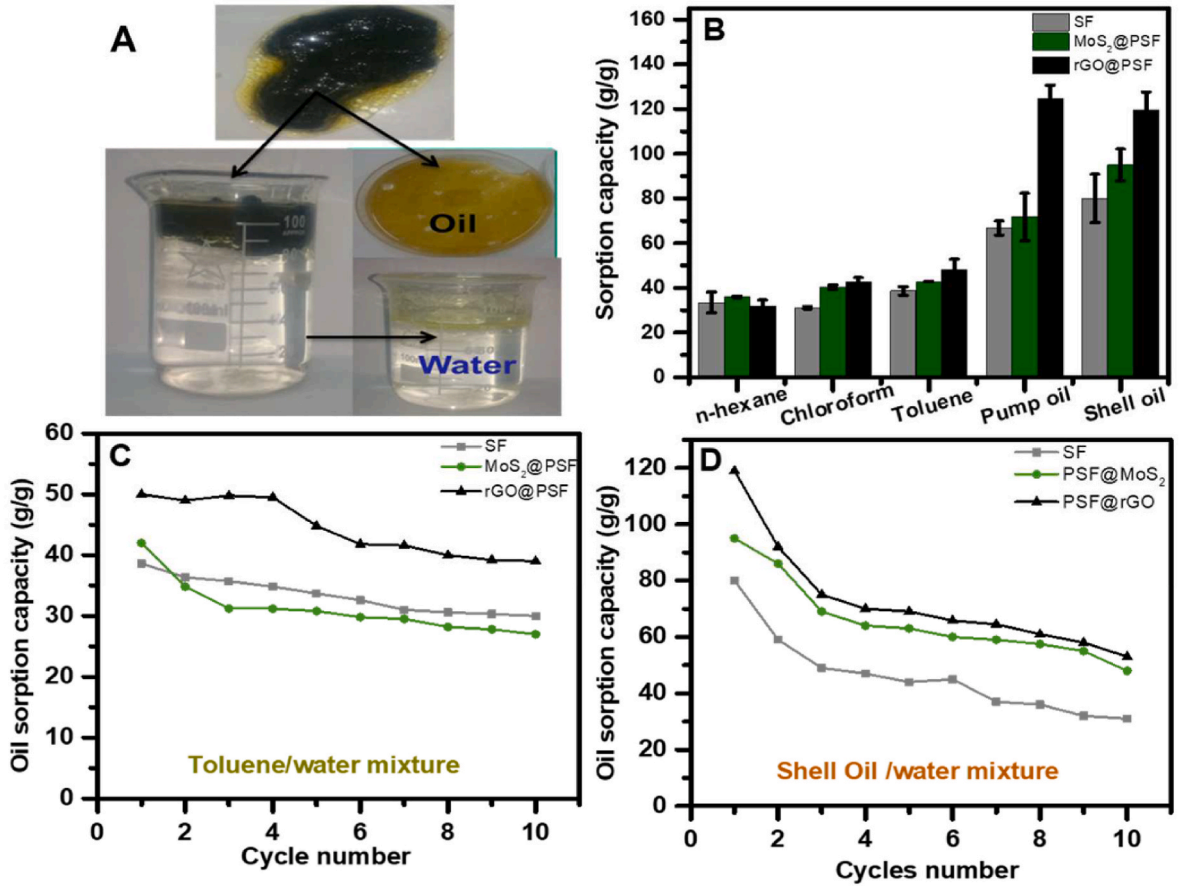

Fig. 6. Adsorption process and recyclability of the pristine and silk-based nanocomposites for oil/water mixtures: (A) Optical images showing selective oil adsorption of rGO@PSF, (B) OSC of rGO@PSF, MoS_2@PSF, and SF for several oils and organic solvents, (C–D) recyclability of rGO@PSF, MoS_2@PSF, and SF over 10 cycles for toluene and shell oil, respectively.

Table 2
Comparison of oil and organic solvent absorption behavior of similar adsorbent materials.

Adsorbent	Type of oil	Oil concentration	OSC (g/g)				Separation efficiency (%)	Reference
Na_2CO_3-degummed silk fibers	Engine oil	1:5 (V_{oil}/V_{water})	9.78				95	[4545]
	Diesel oil		5.55				99	
	Motor oil		5.73				99	
ODA modified silk fibers	Crude oil	1:20 (W_{oil}/W_{water})	46.83				Not available	Patowary et al. (2016)
	Motor oil		84.14					
Raw cotton fibers	Vegetable oil	1:3.57 (V_{oilr}/V_{water})	30				Not available	Deschamps et al. (2003)
rGO@cotton (reduced graphene oxide-coated cotton)	Engine oil	1:4 (V_{oil}/V_{water})	57.01				Not available	(Dashairya et al., 2018)
	Pump oil		53.50					
	Acetone		33.17					
	Propanol		38.27					
	DMF		48.20					
	NMP		41.70					
$NaClO_2$-treated cotton fabric	n-Hexane oil emulsion	1:9 (V_{oil}/V_{water})	Not available				89.4	(Wang et al., 2017a)
	Toluene oil emulsion						92.5	
	Gasoline oil emulsion						90	
	Kerosene oil emulsion						92.2	
	Diesel oil emulsion						89	
rGO@PSF and MoS_2@PSF	n-Hexane	1:4 (V_{oil}/V_{water})	**MoS_2@PSF**	36.02	**rGO@PSF**	31.8	NA	This work
	Toluene			42.84		48.23		
	Chloroform			40.3		42.6		
	Pump oil			72.2		124.6		
	Shell oil			94.8		119.8		
	Crude oil emulsion	10,000/30,00 (mg/l)		2823/ 8018		3051/ 8203	93/99.3 99/98	
	Shell oil emulsion			2251/		2142/	99.5/99.6	
	Pump oil emulsion			3529 743/905		3079 783/906		

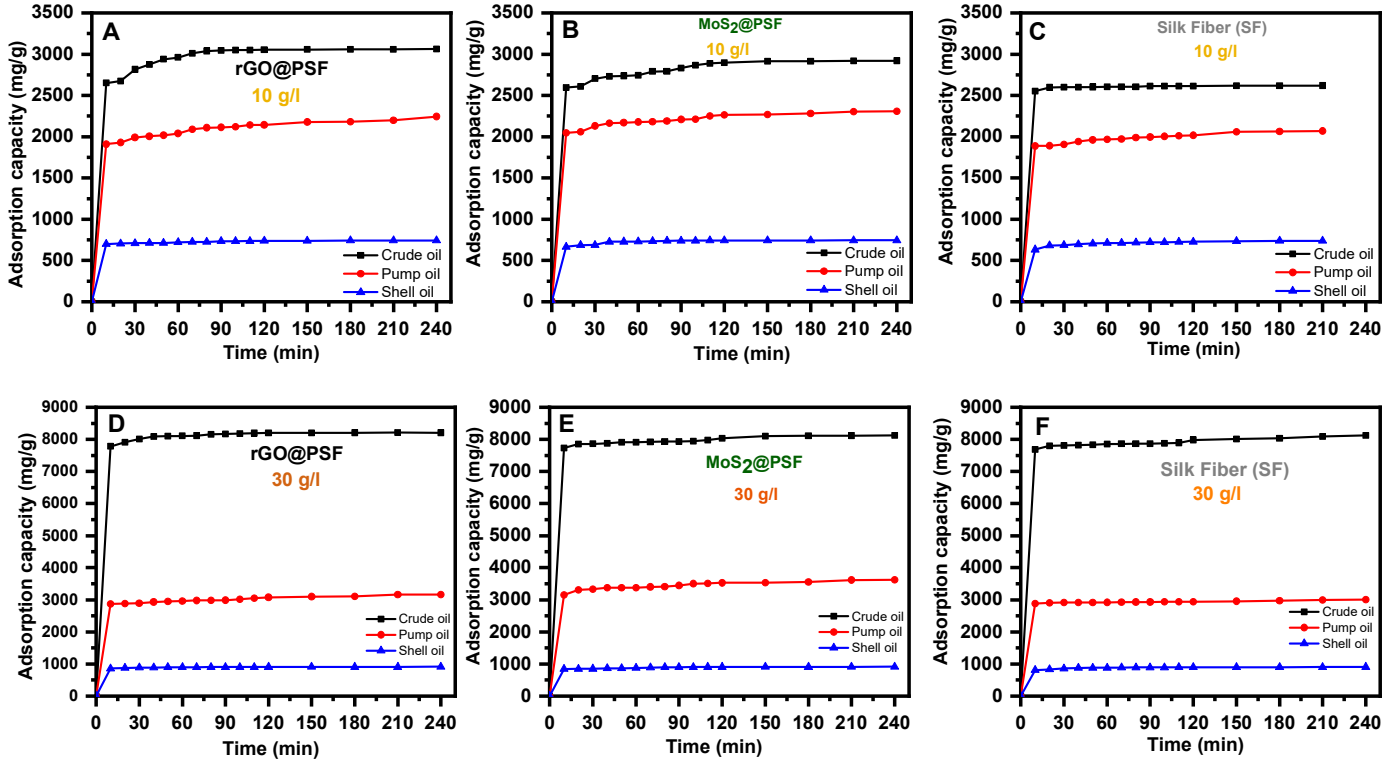

Fig. 7. Separation performance of the pristine and silk-based nanocomposites using three types of oil-in-water emulsions at 318K. Adsorption capacity of oil-in-water emulsions in relation to the contact time at oil content of (A–C) 10 g/l and (D–F) 30 g/l.

capacity was measured by COD and evaluated using eq. (3). Fig. 7 shows emulsion adsorption capacities of SF, rGO@PSF and MoS_2@PSF using different concentration of crude, pump, and shell oils as a function of contact time. In all cases, the adsorption capacity increased with the progression in time until it reaches the equilibrium capacity (approximately after 120 min). It is noteworthy that the equilibrium adsorption capacities increase with the increase of oil concentration from (10–30 g/l) as shown in Fig. 8. Moreover, it was obvious that the adsorption capacity of the rGO@PSF showed a higher performance compared to SF and MoS_2@PSF in case of crude oil-in-water emulsion, whereas for pump oil-in-water emulsion, MoS_2@PSF showed a higher performance than those for SF and rGO@PSF. In addition, crude oil emulsion demonstrated the highest adsorption values among the three types of oil-in-water emulsions. OSC variation may be attributed to the differences in the prepared emulsion droplet size (Table 1). In case of crude oil-in-water emulsion, strong interaction between rGO nanosheets, with the similar sheet size (ca. few hundreds of nanometers, cf Fig. S3C) as crude oil droplet size, leading to perfect occupying of graphene adsorption sites on the surface of SF. On the other hand, pump oil-in-water emulsion has smaller droplet size than crude oil. Hence, the probability of strong interaction on MoS_2 nanosheets (average sheet size of tens of nanometers, cf. Fig. S3D) with pump oil droplets is higher, resulting in better adsorption on MoS_2 active sites on the surface of SF.

Effect of temperature on the separation performance of crude oil-in-water emulsion was performed under three temperatures, i.e. 308K, 318K and 328K. As shown in Fig. S7, adsorption rates increase with increasing the temperature. This may be due to the viscosity of oil-in-water emulsion is negatively related with the increase in temperature, leading to facile diffusion of oil droplets onto the surface of the fibers and increasing the mass transport rate during the different adsorption stages.

To further explore the capability of pristine and silk-based nanocomposites for oil-in-water emulsion separation, Fig. 9 shows photographs and optical microscopy images of the three types of emulsions before and after separation. As shown in (Fig. 9 A, D, G), the feed has a high density of oil droplets crowded all over the section, where no oil droplets were observed in the permeate (Fig. 9 C, F, I). Moreover, as shown in Fig. 9J-L, the DLS values of each corresponding experiment showed the significant reduction in oil droplet size (for feed and permeate) indicating that the emulsions were efficiently separated. Oil removal efficiency of SF, rGO@PSF and MoS_2@PSF at different concentrations of oil-in-water emulsions was shown in Figs. S8A–B. Obviously, rGO@PSF and MoS_2@PSF show excellent removal efficiency for the three types of emulsions, while SF shows lower removal efficiencies for crude oil and pump oil. Table 2 summarizes oil and organic solvent adsorption behavior of similar natural materials that were reported so far. Apparently, the separation performance of oil/water mixtures and oil-in-water emulsions of our developed silk-based nanocomposites are remarkable in comparison with all other reported materials up to now.

3.5.2. Adsorption kinetics

Pseudo-first order (PFO) and pseudo-second order (PSO) kinetic models were utilized to investigate the adsorption kinetics mechanism of oil-in-water emulsion separation. PFO is commonly used to analyze solutes with low concentration (Wang et al., 2019; Huang and Yan, 2018) and could be described as follows.

$$\mathrm{Ln}\ (Qe - Qt) = \mathrm{Ln}Qe - K_1\ t \quad (5)$$

The PSO model supposes the proportional rate of liquid adsorption to

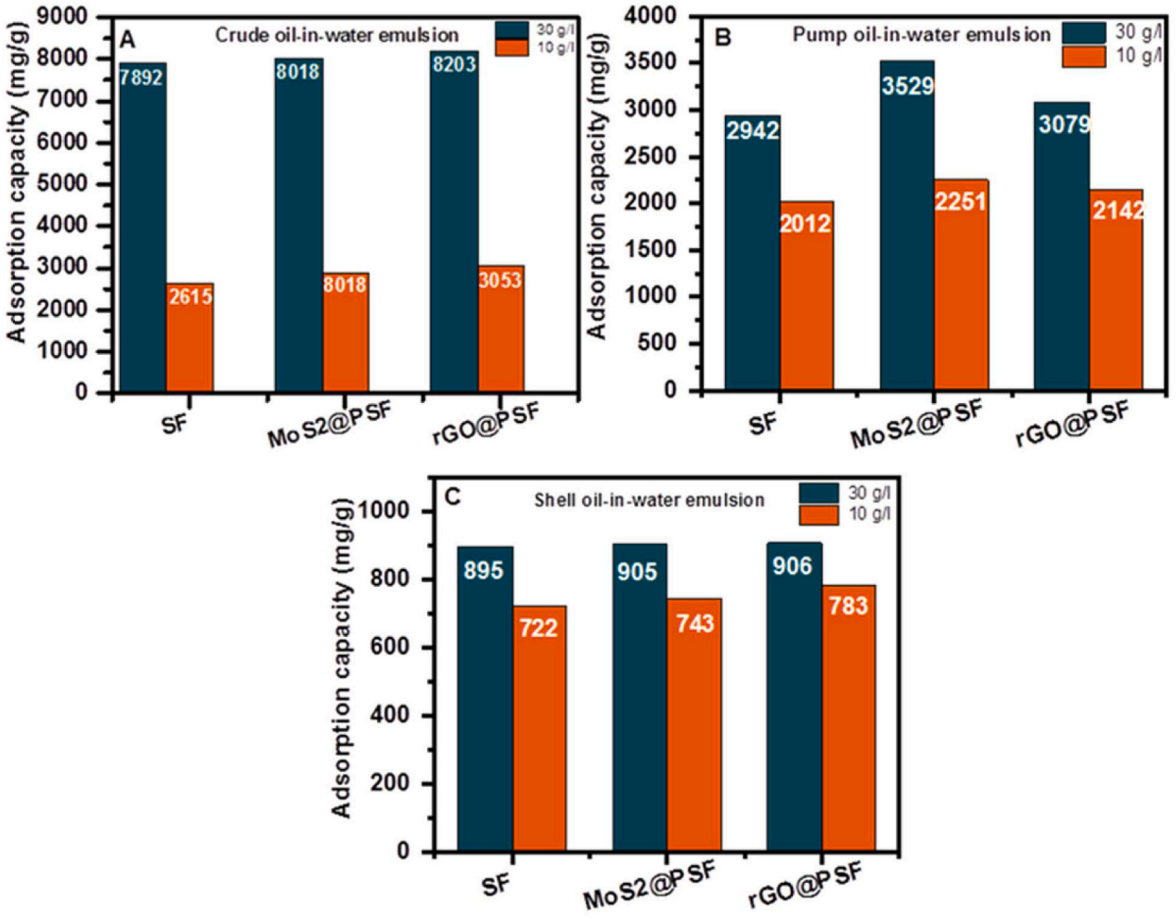

Fig. 8. (A–C) Equilibrium adsorption capacity of the pristine and silk-based nanocomposites against several oil-in-water emulsions of different concentrations.

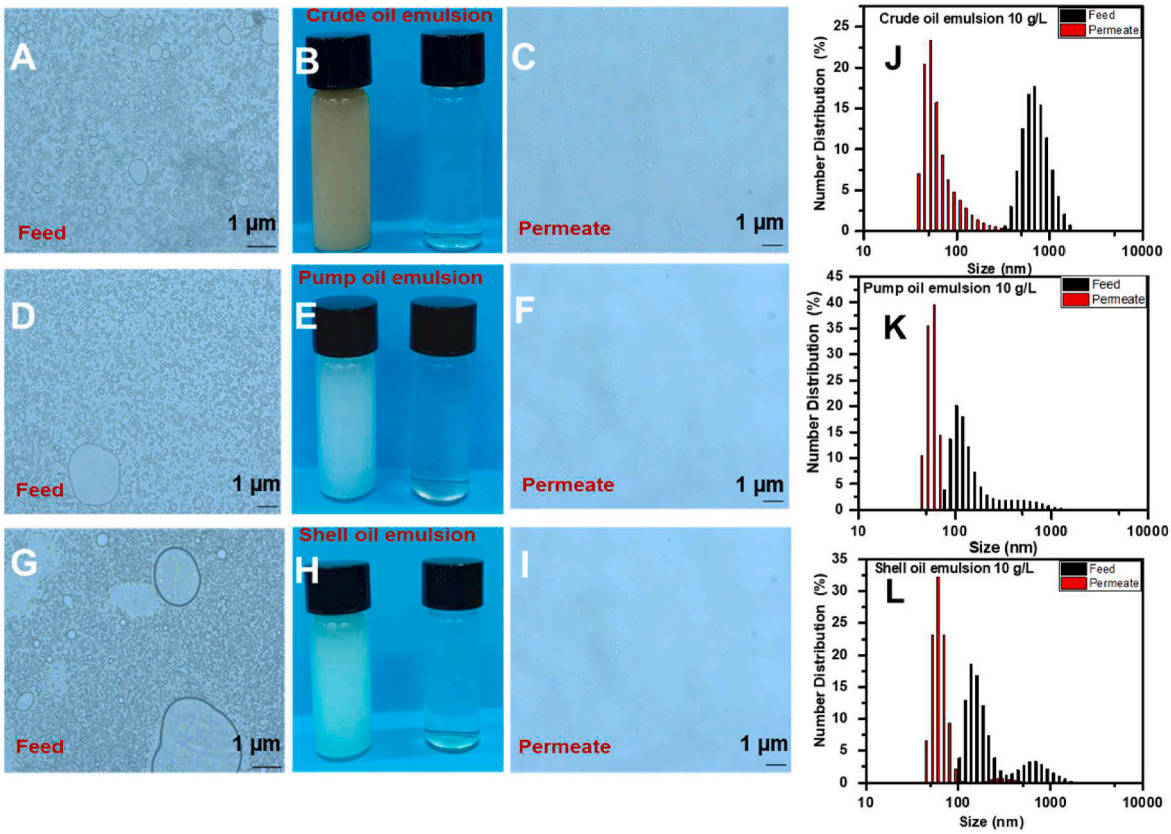

Fig. 9. Optical images of the tested oil-in-water emulsions (10 g/l) before and after separation: (A–C) Crude oil, (D–F) Pump oil, (G–I) Shell oil. Dynamic light scattering (DLS) values of the feed and permeate for (J) Crude oil (K) Shell oil, (L) Pump oil.

the active adsorption sites on the adsorbent surface. PSO could be described as follows (Ho and McKay, 1999):

$$\frac{t}{Q_t} = \frac{1}{K_2 Q_e^2} + \frac{1}{Q_e} \tag{6}$$

where Qe and Qt (mg/g) are the adsorption capacity at time t and the equilibrium adsorption capacity, respectively. K_1, K_2 are the rate constant of the PFO and PSO kinetic models, respectively. The values of K_1, K_2 and Q_e calculate ($Q_{e.cal}$) can be obtained from the fitting line. The coefficient (R^2) was used to evaluate the fitting. The results of PFO and PSO kinetic models performed at 318 °K were concluded in Fig. S9, Fig. S10 and summarized in Tables S1–S3. Moreover, the same behavior was observed for PFO and PSO kinetic models performed at different temperatures as shown in Fig. S11 and Table S4. In case of PSO model, the correlation factor was greater than 0.98. $Q_{e,cal2}$, and Q_e were nearly equal. These results confirm that the PSO kinetic model is better to describe the adsorption mechanism of the oil-in-water emulsions on silk-based nanocomposites.

Arrhenius equation expresses the relationship between reaction rate and temperature. It usually evaluated to distinguish the physical and chemical adsorption processes. A common form of the equation is (Wu, 2007a):

$$Ln\ K2 = -Ea/RT + \ln(A) \tag{7}$$

where, K_2 resembles the rate constant of PSO model, R resembles ideal gas constant (8.314 4621 J K^{-1}/mol), and Ea resembles the active energy (kJ/mol). Fig. 10 exhibits a straight line drawn when plotting lnK_2 against 1/T for a reaction. The slope of an Arrhenius plot is proportional to the activation energy. The activated energy for crude oil-in-water emulsion adsorption on SF, MoS_2@PSF, and rGO@PSF was 15.8, 27.5, and 29.5 kJ/mol, respectively. The Physical and chemical adsorption processes could be identified using the active energy value (Huang and Yan, 2018). Where physical adsorption usually has activation energy ranges from 5 to 40 kJ/mol to achieve equilibrium quickly. The Chemical adsorption, on the other hand, requires a large amount of energy (40–800 kJ/mol). The SF have lower activation energy value, thus more energy would be required (i.e., through an increase in temperature) to reach the top of the reaction (adsorption of the oil droplets).

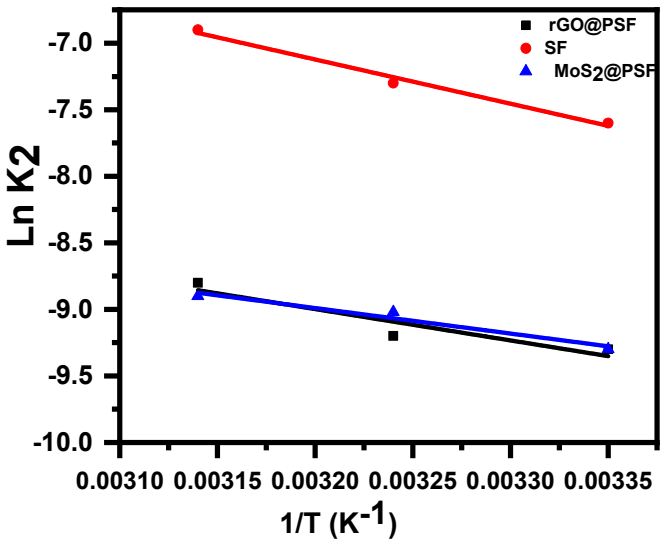

Fig. 10. The relationship between temperature and kinetic rate constant of crude oil-in-water emulsion adsorption onto the pristine and silk-based nanocomposites.

However, in the case of silk-based nanocomposites, the active energy is high enough to reach the top of the reaction and adsorb the oil droplets without additional energy (i.e., at low/room temperature). As a summary, oil adsorption process on the pristine and silk-based nanocomposites is largely controlled by physical adsorption.

In addition, to clarify the rate determining steps and to study the diffusion mechanism of oil-in-water emulsions, intra-particle diffusion (IPD) model was adopted to investigate the kinetics experimental data. IPD can be expressed as follows (Wu, 2007b):

$$Q_t = K_{di}\, t^{0.5} + C \quad (8)$$

where K_{di} is the corresponding IPD rate constant in stage i (=1, 2, 3), mg g^{-1} $min^{-0.5}$ and C is the boundary layers around adsorbents, mg/g. K_{di} and C values are estimated from the slope of Q_t vs. $t^{0.5}$ and intercept, respectively.

Fig. S12 represents the relationship between Q_t and $t^{0.5}$. The plots show multilinearity, indicating that adsorption mechanism for all emulsions occurs over three steps. The adsorption behavior was similar in all cases where, in the first stage (i = 1), the sharply increased line indicating that the adsorption rapidly occurs on the surface of the fibers. In case of crude oil-in-water emulsion, rGO@PSF, showed a higher diffusion rate K_{d1} compared to SF and MoS_2@PSF (Table S5, Table S6 and Table S7). This behavior could be attributed due to the similarity in the size (the same order of magnitude) between the average sheet and the oil droplet size of rGO and crude oil-in-water emulsion. Accordingly, the chance of interaction between crude oil droplets and rGO nanosheets is ideal. By the end of the first stage, the active sites of rGO or MoS_2 nanosheets become mostly occupied. In the second stage (i = 2), the rate slows down since only few active sites are available for the reaction, hence, the competition between oil droplets is relatively high. After long adsorption period over the third stage (i = 3) and, the saturation occurs, and an equilibrium state of the adsorption process is achieved.

3.5.3. Reusability

The recyclability of the pristine and silk-based nanocomposites (SF, rGO@PSF and MoS_2@PSF) for the separation of oil-in-water emulsions was studied to clarify their applicability for oil cleanup application. Fig. 11 shows pump oil-in-water emulsion removal efficiency of SF, rGO@PSF and MoS_2@PSF over ten consecutive adsorption cycles. In case of silk-based nanocomposites, oil removal efficiencies decreased after each consecutive cycle, however still maintaining oil removal efficiencies up to 84% and 83% for MoS_2@PSF and rGO@PSF, respectively after ten cycles. While in case of SF, the oil removal efficiency decreased to 77% after ten cycles. These results indicate the excellent reusability of silk-based nanocomposites even for more than ten cycles of adsorption.

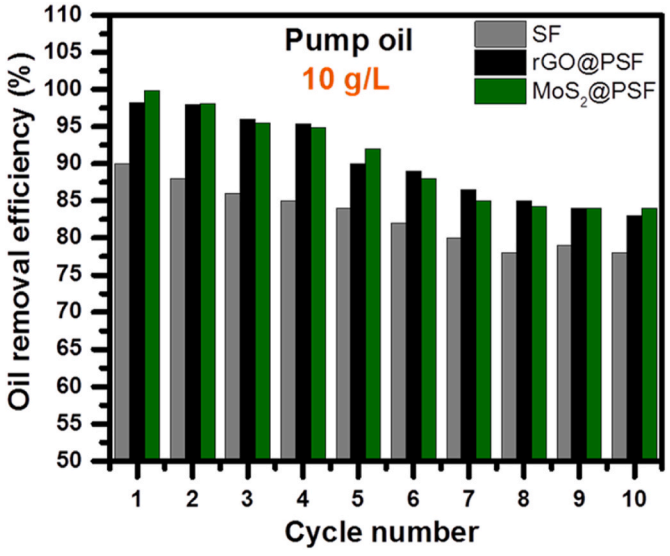

Fig. 11. Recyclability analysis of SF, MoS_2@PSF and rGO@PSF for pump oil-in-water emulsion over ten cycles of adsorption.

Moreover, the reusability of silk-based nanocomposites was investigated by monitoring the stability of rGO@PSF and MoS2@PSF after the recyclability experiments. UV–vis analysis was performed for the permeate resulted after 10th adsorption cycles of oil-in-water emulsion using the silk-based nanocomposites (Fig. S4B). UV–Vis spectra of both samples indicates no absorption peaks associated to rGO or MoS_2 nanosheets indicating the excellent stability of rGO or MoS_2 on the surface of silk fibers.

3.6. Oil adsorption mechanisms

Oil/water mixtures are with complete (or semi complete) phase separation between oil and water layers. The hydrophobic interaction between the micro-sized oil droplets is controlling the initial adsorption phase. Separation mechanism of oil/water mixtures mainly depends on the hydrophobic interactions between oil layers and the surface of SF. In our case, the silk-based nanocomposites attain superhydrophobicity owning to the successful decoration with rGO and MoS_2 nanosheets. These hydrophobic 2D nanosheets showed a high-water repellency, which has a great importance for selective oil absorption from oil/water mixtures. These rGO and MoS_2 nanosheets acted as micro-skimmers for the adsorption of oil droplets, present in the oil/water mixture. The Silk-based nanocomposites remove the oil that is in direct contact with the fibers. The viscosity and concentration of oil and organic solvents influence the adsorption and, subsequently, an accumulation of oil droplets on all available silk fibers may occur.

The separation mechanism of oil-in-water emulsions (Fig. 12) is more sophisticated, and mainly controlled by molecular interactions including hydrophobic and π–π interaction; between oil nanodroplets and rGO and MoS_2 nanosheets that cover the entire surface of the fibers. The most critical factor that breaks down the stability of emulsions is the destruction of the covering (cake) layer present near oil-in-water interfaces. This film layer is characterized by the accumulation of asphaltenes, resins, and naphthenic acids (Liu et al., 2017). The possible demulsification mechanism of oil-in-water emulsion may involve four stages. During the first phase, fibers assemble on surface of water due to superhydrophobicity induced by the decoration with rGO and MoS_2 nanosheets. In the second phase, under vigorous stirring, the fibers derived to sink into the emulsion. Due to the superhydrophobic property of rGO@PSF and MoS_2@PSF and their interactions with the dispersed oil droplets, coalescence and collecting oil droplets onto the fibers might occur, enabling the deposition of oil nanodroplets onto the network of silk fibers. In the third phase, the adsorption process continues where oil droplets are partly separated, however the fibers are not yet fully saturated with oil droplets. In the last phase, the adsorption of the dispersed oil droplets continues on the fibers until full saturation is reached.

4. Conclusions

Novel silk-based nanocomposites were successfully developed though controlled decoration of SF with GO and MoS_2 via a facile immersion method. Oxygen plasma pre-treatment was optimized to promote the adhesion of GO and MoS_2 nanosheets on the entire surface of SF. MoS_2@PSF and rGO@PSF nanocomposites exhibited superhydrophobicity with a water contact angle of ~140° and ~162°, respectively, enabling high selectivity for several heavy oil and organic solvents. The silk-based nanocomposites were tested for the separation of both oil/water mixtures and oil-in-water emulsions and showed unique performance compared to all adsorbents reported so far in literature. rGO@PSF and MoS_2@PSF nanocomposites displayed excellent OSC up to ~120 g/g and ~90 g/g for oil/water mixtures,

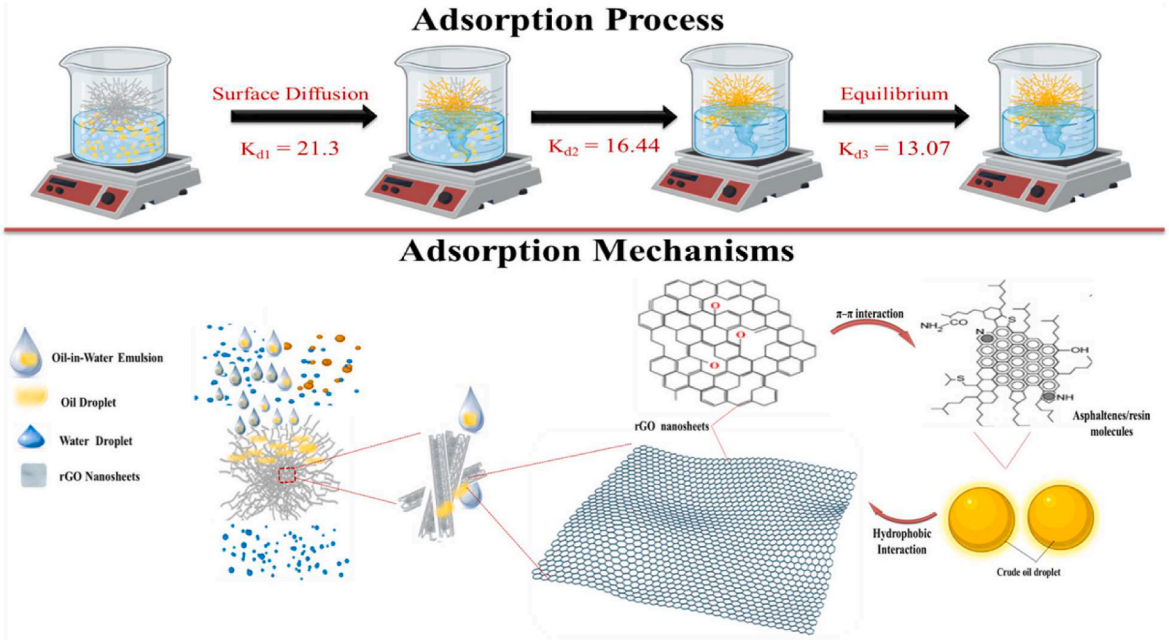

Fig. 12. Adsorption processes and mechanisms for oil-in-water emulsion using the silk-based nanocomposites.

respectively. For the separation of heavy oil-in-water emulsions, rGO@PSF and MoS_2@PSF showed a high separation performance of crude oil-in-water emulsion with OSC up to 8203 and 8018 mg/g, respectively.

CRediT authorship contribution statement

Mohamed K.M. Abd-Elbaki: Formal analysis, Writing – original draft, carried the experiments, data analysis and interpretation, writing the first draft of the manuscript. **Rehab M.G. Ahmed:** Formal analysis, Writing – original draft, carried the experiments, data analysis and interpretation, writing the first draft of the manuscript. **Ahmed S.G. Khalil:** Supervision, Writing – review & editing, of the whole project, reviewing and finalizing the manuscript.

Declaration of competing interest

The authors declare that they have no known competing financial interests or personal relationships that could have appeared to influence the work reported in this paper.

Acknowledgements

Ahmed S. G. Khalil acknowledges the financial support received from the Arab-German Academy of Sciences and Humanities (AGYA), Germany.

Appendix A. Supplementary data

Supplementary data to this article can be found online at https://doi.org/10.1016/j.jclepro.2022.132707.

References

Abdel-Aty, Ahmed, A.R., et al., 2020. High performance isotropic polyethersulfone membranes for heavy oil-in-water emulsion separation. Separ. Purif. Technol. 253, 117467.
Aboutalebi, Hamed, Seyed, et al., 2011. Spontaneous formation of liquid crystals in ultralarge graphene oxide dispersions. Adv. Funct. Mater. 21, 2978–2988, 15.
Alam, A.K.M.M., Shubhra, Q.T., Al-Imran, G., Barai, S., Islam, M.R., Rahman, M.M., 2011. Preparation and characterization of natural silk fiber-reinforced polypropylene and synthetic E-glass fiber-reinforced polypropylene composites: a comparative study. J. Compos. Mater. 45 (22), 2301–2308. .
Ali, Basant A., et al., 2019. Untapped potential of polymorph MoS2: tuned cationic intercalation for high-performance symmetric supercapacitors. ACS Appl. Mater. Interfaces 11, 33955–33965, 37.
Anis, Badawi, et al., 2017a. Tuning the plasmon resonance and work function of laser-scribed chemically doped graphene. Carbon 120, 44–53. .
Anis, Badawi, et al., 2017b. Tuning the plasmon resonance and work function of laser-scribed chemically doped graphene. Carbon 120, 44–53.
Babu, K. Murugesh, 2018. Silk: Processing, Properties and Applications. Woodhead Publishing, .
Badawi, Anis, Hesham El Fllah, Tawfik Ismail, Wael M.Fathallah, A.S.G. Khalil, O.M. Hemeda, Yehia A. Badr, 2020, Preparation, characterization, and thermal conductivity of polyvinyl-formaldehyde/MWCNTs foam: a low cost heat sink substrate,J. Mater. Res. Technol., 9, 3, Pages 2934-2945.
Benavente, E., et al., 2002. Intercalation chemistry of molybdenum disulfide. Coord. Chem. Rev. 224, 87–109, 1-2.
Bhattacharyya, Subhes C., Andon, Blake, 2009. Domestic demand for petroleum products in MENA countries. Energy Pol. 37, 1552–1560, 4.
Bullock, Robin J., Perkins, Robert A., Aggarwal, Srijan, 2019. In-situ Burning with Chemical Herders for Arctic Oil Spill Response: Meta-Analysis and Review. Science of The Total Environment, p. .
Cao, Yang, Wang, Bochu, 2009. Biodegradation of silk biomaterials, 4 Int. J. Mol. Sci. 10, 1514–1524. .
Cao, Enjuan, et al., 2018. Metallic nanoparticles roughened Calotropis gigantea fiber enables efficient absorption of oils and organic solvents. Ind. Crop. Prod. 115, 272–279.
Chang, Kun, et al., 2016. Targeted synthesis of 2H-and 1T-phase MoS2 monolayers for catalytic hydrogen evolution, 45 Adv. Mater. 28, 10033–10041. .
Chen, Fujia, Porter, David, Fritz, Vollrath, 2012a. Structure and physical properties of silkworm cocoons, 74 J. R. Soc. Interface 9, 2299–2308. .
Chen, Fujia, Porter, David, Fritz, Vollrath, 2012b. Morphology and structure of silkworm cocoons. Mater. Sci. Eng. C 32, 772–778, 4.
Chen, Chun-Hui, et al., 2018. Hydrophobic lipophilic modified cotton fabric for oil absorption applications. J. Nat. Fibers.
Chen, Shaoyong, et al., 2019. Mechanical properties of Bombyx mori silkworm silk fibre and its corresponding silk fibroin filament: a comparative study. Mater. Des. 181, 108077.
Conrad, Kevin, Cleland, Rea, Reyes, Nicholas, 2021. Health Consequences of Marine Oil Spills: Lessons Learned from the Deepwater Horizon Accident." from Hurricanes to Epidemics. Springer, Cham, pp. 27–37.
Dashairya, Love, Rout, Madhabendra, Saha, Partha, 2018. Reduced graphene oxide-coated cotton as an efficient absorbent in oil-water separation. Adv. Compos. Hybrid Mater. 1, 135–148, 1.
Deschamps, Gerald, et al., 2003. Oil removal from water by selective sorption on hydrophobic cotton fibers. Study of sorption properties and comparison with other cotton fiber-based sorbents. Environ. Sci. Technol. 37, 1013–1015, 5.
Duan, Haonan, et al., 2021. Superhydrophobic-superoleophilic biochar-based foam for high-efficiency and repeatable oil-water separation. Sci. Total Environ. 780, 146517.
Fang, Kuanjun, et al., 2008. Inkjet printing effects of pigment inks on silk fabrics surface-modified with O2 plasma. J. Appl. Polym. Sci. 107, 2949–2955, 5.

Farooq, Umer, Ingrid, C., 2018. Taban, and Per S. Daling. "Study of the oil interaction towards oil spill recovery skimmer material: effect of the oil weathering and emulsification properties. Mar. Pollut. Bull. 135, 119–128. .
Geng, Yan, Wang, Shu Jun, Kim, Jang-Kyo, 2009. Preparation of graphite nanoplatelets and graphene sheets. J. Colloid Interface Sci. 336, 592–598, 2.
Geng, Xiumei, et al., 2016. Pure and stable metallic phase molybdenum disulfide nanosheets for hydrogen evolution reaction, 1 Nat. Commun. 7, 1–7. .
Gore, Prakash M., et al., 2019a. Progress in silk materials for integrated water treatments: fabrication, modification and applications. Chem. Eng. J.
Gore, Prakash M., et al., 2019b. Silk fibres exhibiting biodegradability & superhydrophobicity for recovery of petroleum oils from oily wastewater. J. Hazard Mater., 121823
Gupta, Ankur, et al., 2016. Nanoemulsions: formation, properties and applications. Soft Matter 12, 2826–2841, 11.
Gupta, Raju Kumar, et al., 2017. Oil/water separation techniques: a review of recent progresses and future directions. J. Mater. Chem. A 5, 16025–16058, 31.
He, Xiaobo, et al., 2019. Bulk" 1T/2H-MoS2 with tunable phases and residual S, N Co-doped carbon as a highly active and durable catalyst for hydrogen evolution. ACS Appl. Energy Mater. 2, 2022–2033, 3.
Ho, Yuh-Shan, McKay, Gordon, 1999. Pseudo-second order model for sorption processes. Process Biochem. 34, 451–465, 5.
Hodak, Satreerat K., et al., 2008. Enhancement of the hydrophobicity of silk fabrics by SF6 plasma. Appl. Surf. Sci. 254, 4744–4749, 15.
Huang, J., Yan, Z., 2018. Adsorption mechanism of oil by resilient graphene aerogels from oil-water emulsion. Langmuir 34, 1890–1898.
Jao, Dave, Mou, Xiaoyang, Hu, Xiao, 2016. Tissue regeneration: a silk road. J. Funct. Biomater. 7, 22, 3.
Jeong, Lim, et al., 2009. Plasma-treated silk fibroin nanofibers for skin regeneration, 3 Int. J. Biol. Macromol. 44, 222–228. .
Kukkar, Deepak, et al., 2020. Recent advances in carbon nanotube sponge–based sorption technologies for mitigation of marine oil spills. J. Colloid Interface Sci. .
Langangen, Øystein, et al., 2017. The effects of oil spills on marine fish: implications of spatial variation in natural mortality. Mar. Pollut. Bull. 119, 102–109, 1.
Liu, Juan, et al., 2017. Recyclable magnetic graphene oxide for rapid and efficient demulsification of crude oil-in-water emulsion. Fuel 189, 79–87.
Liu, Yunqiu, et al., 2020a. Use of Nano-TiO2 self-assembled flax fiber as a new initiative for immiscible oil/water separation. J. Clean. Prod. 249, 119352.
Liu, Yunqiu, et al., 2020b. Use of Nano-TiO2 self-assembled flax fiber as a new initiative for immiscible oil/water separation. J. Clean. Prod. 249, 119352.
Liu, Shuai, et al., 2021. Gold nanoparticles modified graphene foam with superhydrophobicity and superoleophilicity for oil-water separation. Sci. Total Environ. 758, 143660.
Long, Sishi, et al., 2021. Renewable and robust biomass carbon aerogel derived from deep eutectic solvents modified cellulose nanofiber under a low carbonization temperature for oil-water separation. Separ. Purif. Technol. 254, 117577.
Ma, Han, Shen, Zhigang, Ben, Shuang, 2018. Understanding the exfoliation and dispersion of MoS2 nanosheets in pure water. J. Colloid Interface Sci. 517, 204–212. .
Mao, Min, et al., 2021. Mechanically flexible, super-hydrophobic and flame-retardant hybrid nano-silica/graphene oxide wide ribbon decorated sponges for efficient oil/water separation and fire warning response. Compos. Appl. Sci. Manuf. 140, 106191. .
Mohammed, Yosef, Alaa Fahmy, Walid El Hotaby, Ali M.Hassana Ahmed S.G.Khalil, Badawi Anis, 2020, High performance graphene-based PVF foam for lead removal from water, J. Mater. Res. Technol., Volume 9, Issue 5, Pages 11861-11875.
Monti, P., et al., 1998. Raman spectroscopic studies of silk fibroin from Bombyx mori. J. Raman Spectrosc. 29, 297–304, 4.
Nine, Md J., et al., 2020. Superhydrophobic/superoleophilic natural fibres for continuous oil-water separation and interfacial dye-adsorption. Separ. Purif. Technol. 233, 116062. .
Omar, Asmaa M., et al., 2019. Revealing the role of the 1T phase on the adsorption of organic dyes on MoS 2 nanosheets, 49 RSC Adv. 9, 28345–28356. .
Omar, Asmaa MA., et al., 2021. Construction of 2D layered TiO2@ MoS2 heterostructure for efficient adsorption and photodegradation of organic dyes. Nanotechnology 32, 335605, 33.
Pal, Sukanta, Mondal, Sourav, Maity, Jayanta, 2019. Fabrication of thin fluoropolymer adhered cotton fabric surface for efficiently microscopic to macroscopic level oil/water separation. Surf. Topogr. Metrol. Prop. 7, 025001, 2.
Patowary, Manoj, Pathak, Khanindra, Ananthakrishnan, Rajakumar, 2016. Robust superhydrophobic and oleophilic silk fibers for selective removal of oil from water surfaces. RSC Adv. 6, 73660–73667, 77.
Peng, Min, et al., 2018. Superhydrophobic kaolinite modified graphene oxide-melamine sponge with excellent properties for oil-water separation. Appl. Clay Sci. 163, 63–71. .
Prince, Roger C., Butler, Josh D., 2014. A protocol for assessing the effectiveness of oil spill dispersants in stimulating the biodegradation of oil, 16 Environ. Sci. Pollut. Control Ser. 21, 9506–9510. .
Qi, Yuhang, et al., 2016. CO2-induced phase engineering: protocol for enhanced photoelectrocatalytic performance of 2D MoS2 nanosheets, 2 ACS Nano 10, 2903–2909. .
Radetic, Maja, et al., 2008. Efficiency of recycled wool-based nonwoven material for the removal of oils from water, 3 Chemosphere 70, 525–530. .
Rani, K. Vinisha, Sarma, Bornali, Sarma, Arun, 2018a. Plasma treatment on cotton fabrics to enhance the adhesion of Reduced Graphene Oxide for electro-conductive properties. Diam. Relat. Mater. 84, 77–85.
Rani, K. Vinisha, Sarma, Bornali, Sarma, Arun, 2018b. Plasma treatment on cotton fabrics to enhance the adhesion of Reduced Graphene Oxide for electro-conductive properties. Diam. Relat. Mater. 84, 77–85.
Rehab M.G. Ahmed, Badawi Anis, Ahmed S.G. Khalil, 2021. Facile surface treatment and decoration of graphene-based 3D polymeric sponges for high performance separation of heavy oil-in-water emulsions, J. Chem. Environ. Eng. , 9, 2, April 2021, 105087.
Ren, F., Zhu, Z., Li, J., 1997. Nutritious Foodstuff-Silk Extract Made from Natural Silk and Making Method. China Patent. CN1152410A.
Rockwood, Danielle N., et al., 2011. Materials fabrication from Bombyx mori silk fibroin. Nat. Protoc. 6, 1612, 10.
Ron, Eliora Z., Rosenberg, Eugene, 2014. Enhanced bioremediation of oil spills in the sea. Curr. Opin. Biotechnol. 27, 191–194. .
Saric, Merisa, Scheibel, Thomas, 2019. Engineering of silk proteins for materials applications. Curr. Opin. Biotechnol. 60, 213–220. .
Saththasivam, Jayaprakash, Loganathan, Kavithaa, Sarp, Sarper, 2016. An overview of oil–water separation using gas flotation systems. Chemosphere 144, 671–680. .
Schrope, Mark, 2010. A scientist at the centre of the spill: vernon Asper was one of the first researchers in the Gulf of Mexico to study the oil gushing out from the BP well. But it has not all been smooth sailing. Nature 466, 680–685, 7307.
Seo, Young Kwon, et al., 2007. The biocompatibility of silk scaffold for tissue engineered ligaments. Key Eng. Mater. 342. Trans Tech Publications Ltd.
Sun, Xiaoming, et al., 2008. Nano-graphene oxide for cellular imaging and drug delivery, 3 Nano Res. 1, 203–212. .
Taşdemir, Münir, et al., 2010. Investigation of properties of polymer/textile fiber composites. Int. J. Polym. Mater. 59, 200–214, 3.
Tan, Xuefei, et al., 2020. Superhydrophobic/superoleophilic Corn Straw as an Eco-Friendly Oil Sorbent for the Removal of Spilled Oil. Clean Technologies and Environmental Policy, pp. 1–8. .
Thema, F.T., et al., 2013. Synthesis and characterization of graphene thin films by chemical reduction of exfoliated and intercalated graphite oxide. J. Chem. 2013.
Wang, Jintao, et al., 2017. Hydrothermal fabrication of robustly superhydrophobic cotton fibers for efficient separation of oil/water mixtures and oil-in-water emulsions. J. Ind. Eng. Chem. 54, 174–183.
Wang, Chih-Feng, et al., 2018. Toward superhydrophobic/superoleophilic materials for separation of oil/water mixtures and water-in-oil emulsions using phase inversion methods. Coatings 8, 396, 11.
Wang, S., Ning, H., Hu, N., Huang, K., Weng, S., Wu, X., Wu, L., Liu, J., Alamusi, 2019. Preparation and characterization of graphene oxide/silk fbroin hybrid aerogel for dye and heavy metal adsorption. Compos. B Eng. 163, 716–722.
Wang, Wen Yi, et al., 2020. The effect of plasma pretreatment of dyeability of silk with acid dye. Trans Tech Publications Ltd Key Eng. Mater. 831.
Wang, Hai-Yan, Zhang, Yu-Qing, Wei, Zheng-Guo, 2021. Dissolution and processing of silk fibroin for materials science, 3 Crit. Rev. Biotechnol. 41, 406–424. .
Wu, Chung-Hsin, 2007a. Adsorption of reactive dye onto carbon nanotubes: equilibrium, kinetics and thermodynamics, 93-100 J. Hazard Mater. 144, 1–2. .
Wu, Chung-Hsin, 2007b. Adsorption of reactive dye onto carbon nanotubes: equilibrium, kinetics and thermodynamics. J. Hazard Mater. 144, 1–2, 93-100.
Wu, Zhen-Yu, et al., 2014. Carbon nanofiber aerogels for emergent cleanup of oil spillage and chemical leakage under harsh conditions. Sci. Rep. 4, 4079.
Xia, Chengbo, et al., 2018. Facile one-pot synthesis of superhydrophobic reduced graphene oxide-coated polyurethane sponge at the presence of ethanol for oil-water separation. Chem. Eng. J. 345, 648–658. .
Xiao, Weilong, et al., 2021. Fabrication of foam-like oil sorbent from polylactic acid and Calotropis gigantea fiber for effective oil absorption. J. Clean. Prod. 278, 123507.
Xu, Weijie, Ma, Junyu, Jabbari, Esmaiel, 2010a. Material properties and osteogenic differentiation of marrow stromal cells on fiber-reinforced laminated hydrogel nanocomposites, 6 Acta Biomater. 6, 1992–2002. .
Xu, Weijie, Ma, Junyu, Jabbari, Esmaiel, 2010b. Material properties and osteogenic differentiation of marrow stromal cells on fiber-reinforced laminated hydrogel nanocomposites, 6 Acta Biomater. 6, 1992–2002. .
Yamada, A.K.I.K.O., 1998. The absorbing rate of moisture for silk fabric comparing to other fabrics made from various fibers. J. Seric. Sci. Jpn. 67 (4), 333–339.
Yan, Luke, et al., 2020. CNTs/TiO2 composite membrane with adaptable wettability for on-demand oil/water separation. J. Clean. Prod. 275, 124011.
Yu, Yifu, et al., 2018. High phase-purity 1T′-MoS 2-and 1T′-MoSe 2-layered crystals. Nat. Chem. 10, 638–643, 6.
Zhang, Hongyuan, et al., 2019. Super light 3D hierarchical nanocellulose aerogel foam with superior oil adsorption. J. Colloid Interface Sci. 536, 245–251. .
Zhou, Shuai, et al., 2016. One-pot synthesis of robust superhydrophobic, functionalized graphene/polyurethane sponge for effective continuous oil–water separation. Chem. Eng. J. 302, 155–162. .
Zhou, Jian, et al., 2019. Silk fibroin-graphene oxide functionalized melamine sponge for efficient oil absorption and oil/water separation. Appl. Surf. Sci. 497, 143762.
Zhou, Lei, et al., 2020. MoS 2-roughened hollow-lumen plant fibers with enhanced oil absorption capacity. Cellulose 27, 2267–2278, 4.
Zhu, Ke, et al., 2013. Oil spill cleanup from sea water by carbon nanotube sponges. Front. Mater. Sci. 7, 170–176, 2.
Zulan, Liu, et al., 2019. Reduced graphene oxide coated silk fabrics with conductive property for wearable electronic textiles application. Adv. Electron. Mater. 5, 1800648, 4.